Domain-Adaptive Crowd Counting via High-Quality Image Translation and Density Reconstruction

Junyu Gao, *Member, IEEE*, Tao Han, *Student Member, IEEE*, Yuan Yuan, *Senior Member, IEEE*, and Qi Wang, *Senior Member, IEEE*

***Abstract*— Recently, crowd counting using supervised learning achieves a remarkable improvement. Nevertheless, most counters rely on a large amount of manually labeled data. With the release of synthetic crowd data, a potential alternative is transferring knowledge from them to real data without any manual label. However, there is no method to effectively suppress domain gaps and output elaborate density maps during the transferring. To remedy the above problems, this article proposes a domain-adaptive crowd counting (DACC) framework, which consists of a high-quality image translation and density map reconstruction. To be specific, the former focuses on translating synthetic data to realistic images, which prompts the translation quality by segregating domain-shared/independent features and designing content-aware consistency loss. The latter aims at generating pseudo labels on real scenes to improve the prediction quality. Next, we retrain a final counter using these pseudo labels. Adaptation experiments on six real-world datasets demonstrate that the proposed method outperforms the state-of-the-art methods.**

***Index Terms*— Crowd counting, domain adaptation, image translation.**

I. Introduction

CROWD counting is usually treated as a pixel-level estimation problem, which predicts the density value for each pixel and sums the entire prediction map as a final counting result. A pixelwise density map produces more detailed information than a single number for a complex crowd scene. In addition, it also boosts other highly semantic crowd analysis (group detection [1]–[3], crowd segmentation [4], public management [5], and so on) or video surveillance tasks (video summarization [6]–[8] and abnormal detection [9]). Recently, benefiting from the powerful capacity of deep learning, there is a significant promotion in the field of counting. However, currently released datasets are too small to satisfy the mainstream deep learning-based methods [10]–[15]. The main reason is that constructing a large-scale crowd counting dataset is extremely demanding, which needs many human resources [16].

To handle the scarce data problem, many researchers pay attention to data generation. Exploiting computer graphics to render photorealistic crowd scenes becomes an alternative to generate a large-scale dataset [17]. Unfortunately, due to the differences between the synthetic and real worlds (also named "domain shifts/gap"), there is an obvious performance degradation when applying the synthetic crowd model to the real world. For reducing the domain shifts, Wang *et al.* [17] are the first to propose a crowd counting via domain adaptation method based on CycleGAN [18], which translates synthetic data to photorealistic scenes and then apply the trained model in the wild. In this article, we also focus on domain-adaptive crowd counting (DACC), which attempts to transfer the useful knowledge for crowd counting from a source domain (the synthetic data) to a target domain (the real world).

However, there are two problems in the CycleGAN-style [17]–[20] adaptation methods. First, output some distorted translations and lose many textures and local structured patterns (these features are key characteristics for congested crowd scenes), which produces coarse density map. The left box in Fig. 1 shows the three types of false cases (red: lost textures, green: distorted data, and blue: lost local pattern). Second, mistakenly estimate response values for unseen background objects in the target domain so that the prediction map is very coarse and inaccurate. The right box in Fig. 1 demonstrates some misestimations of the background.

For the first problem, the main reason is that CycleGAN only classifies the translated and recalled results at the image level and treats image translation as an entire process. In practice, we find that different domains have common crowd contents, namely, person's structure features and crowd distribution patterns, which is regarded as "domain-shared features." Besides, different domains have their own unique scene attributes, named "domain-independent features," which may be caused by different factors such as backgrounds and sensors' setting. Motivated by this discovery, we propose a two-step chain architecture to segregate the two types of features, named interdomain features segregation (IFS). It first extracts domain-shared features f. Next, by decorating f with the domain-independent features of domain $\mathcal{T}$, IFS reconstructs the like-$\mathcal{T}$ images. For further maintaining the local patterns and texture features, we carefully design multiscale adversarial translation loss and content-aware loss.

Manuscript received 12 January 2021; revised 6 August 2021; accepted 22 October 2021. Date of publication 12 November 2021; date of current version 4 August 2023. This work was supported by the National Natural Science Foundation of China under Grant U1864204, Grant 61773316, Grant 61632018, and Grant 61825603. *(Corresponding author: Qi Wang.)*

The authors are with the School of Artificial Intelligence, Optics and Electronics (iOPEN), Northwestern Polytechnical University, Xi'an, Shaanxi 710072, China (e-mail: gjy3035@gmail.com; hantao10200@mail.nwpu.edu.cn; y.yuan1.ieee@gmail.com; crabwq@gmail.com).

This article has supplementary material provided by the authors and color versions of one or more figures available at https://doi.org/10.1109/TNNLS.2021.3124272.

Digital Object Identifier 10.1109/TNNLS.2021.3124272

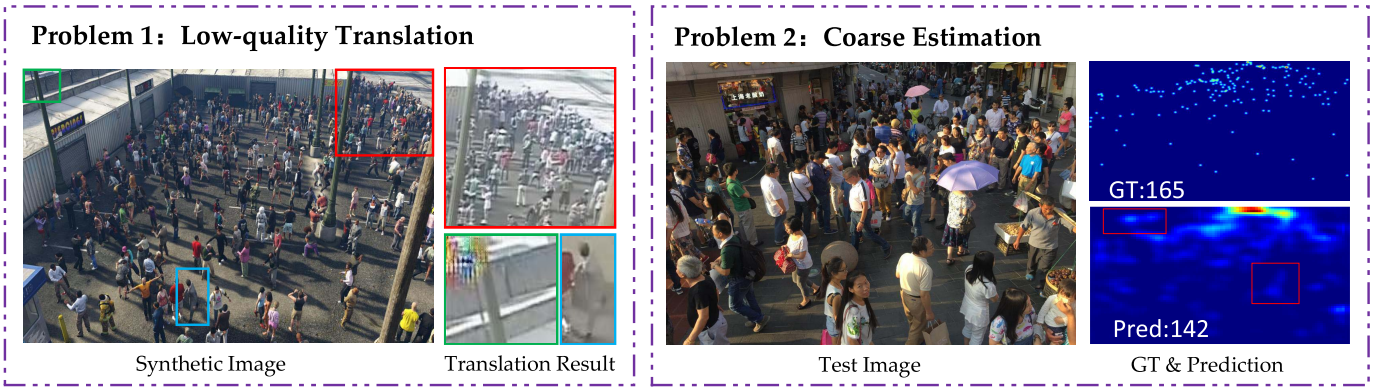

Fig. 1. Existing problems in the current DACC.

Compared with the traditional adversarial loss and Cycle loss, the proposed losses can significantly reduce distortions and retain image contents during the translation.

For the second problem, we present a retraining scheme based on the density reconstruction. In the counting field, the ground truth of density map is generated by using a Gaussian kernel from the head position. According to this prior, we attempt to find the most likely locations of heads by comparing the similarity between the coarse map and the standard Gaussian kernel. Consequently, pseudo density maps are reconstructed. Then, a final counter is trained on the target images and the pseudo maps, which performs better in the real world than the coarse model.

As a summary, the key contributions of this article are as follows.

1) Propose a two-step image translation to segregate inter-domain features, and design two effective types of losses, which can extract/retain crowd contents and yield high-quality photorealistic crowd images.
2) Exploit Gaussian prior to reconstruct pseudo labels according to the coarse results. Based on them, retrain a fine counter to further enhance the density quality and counting performance.
3) The proposed method outperforms the state-of-the-art results in the DACC from synthetic data to the real world.

II. Related Works

A. Crowd Counting

1) Supervised Learning: Early methods for crowd counting focus on extracting handcrafted features (such as Harr [21], HOG [22], and texture features [23]) to regress the number of people [24]–[26]. Recently, many object counting studies are based on convolution neural network (CNN) methods. Some researchers design network structures to enhance multiscale feature extraction capabilities [27], [28]. Zhang *et al.* [27] proposed a multicolumn CNN by combining different kernel sizes. Onoro-Rubio and López-Sastre [28] presented a multiscale Hydra CNN, which performs the density prediction in different scenes. Some works [29]–[32] exploit contextual information to boost counting performance. Sindagi and Patel [29] extracted global and local feature to aid the density estimation, and Liu *et al.* [30] presented a context-aware CNN, designing a multistream with different respective fields after a VGG backbone. The rest works [33]–[35] fuse multistage features to achieve accurate counting. Idrees *et al.* [33] combined the results of different stages to predict the density map and head localization. Jiang *et al.* [34] designed a trellis encoder–decoder architecture to incorporate the features from multiple decoding paths. Liu *et al.* [35] presented a structured feature enhancement module (SFEM) using conditional random field (CRF) to refine the features of different stages.

2) Counting for Scarce Data: In addition to the aforementioned supervised methods, some approaches dedicate to handling the problem of scarce data. Wang *et al.* [17] constructed a large-scale synthetic crowd dataset, including more than 15 000 images and ∼7.5 million instances. Recently, two real-world crowd datasets are released, namely, JHU-CROWD [36] (4250 images and ∼1.1 million instances) and Crowd Surveillance [37] (13 945 images and ∼0.4 million annotations). By comparing them, the amount of labeled real data is far from that of synthetic data. Besides, collecting and annotating real data is an expensive and difficult assignment. Thus, some researchers remedy this problem from the methodology. Liu *et al.* [38] proposed a self-supervised ranking scheme as an auxiliary to improve performance. Sam *et al.* [39] presented an almost unsupervised method, of which 99.9% parameters in the proposed autoencoder are trained without any label. Olmschenk *et al.* [40] enlarged the data by utilizing generative adversarial networks (GANs). To fully escape from manually labeled data and simultaneously attain an accepted result, Wang *et al.* [17] presented a crowd counting via domain adaptation method, which is easy to land in practice from the perspectives of performance and costs.

B. Domain-Adaptive Vision Tasks

Considering that there are not many works about domain adaptation in crowd counting, thus, this section reviews other applications, such as classification and segmentation. Some methods [41]–[43] adopt the Maximum mean discrepancy [44] to alleviate domain shift in the field of image classification. After some synthetic segmentation datasets [45], [46] are released, a few works [47]–[50] adopt adversarial learning to reduce the pixelwise domain gap. Benefiting from the power of

TABLE I
SOME BEFOREHAND ANNOTATIONS OF INVOLVED SYMBOL

Symbol	Explanation
$\mathcal{S}$	source domain (synthetic data)
$\mathcal{T}$	target domain (real-world data)
$\boldsymbol{G}_c$	domain-shared feature extractor (see Fig. 2)
$\boldsymbol{G}_{to\mathcal{S}}$	source domain decoder (see Fig. 2)
$\boldsymbol{G}_{to\mathcal{T}}$	target domain decoder (see Fig. 2)
$\boldsymbol{D}_c$	domain-shared feature discriminator (see Fig. 2)
$\boldsymbol{D}_{to\mathcal{S}}$	source domain discriminator (see Fig. 2)
$\boldsymbol{D}_{to\mathcal{T}}$	target domain discriminator (see Fig. 2)

CycleGAN [18], some scholars [19], [20] utilize it to translate synthetic images to realistic data. Recently, some researchers attempt to disentangle the image content and style to translate images [51]–[54]. From these works for image classification and segmentation tasks, they only focus on global styles and object-level structures. For counting task, in addition to the style and structures, we also devote to preserving the consistency of local pattern and textures. Thus, we start from the translation architecture and loss designation to achieve our goal.

1) Different From the Traditional Segregation Methods [52], [55]: This extracts a simple domain code to generate images; in order to reconstruct the image details, we use two different generators that contain a large number of neurons. The richer domain-independent attributes are stored in the generators than the simple domain code.

2) Different From the Previous Cycle-Consistent Methods [18]–[20]: This only constrains the original image and the recalled image by a cycle-consistent loss: to maintain the key content during the translation process, we should regularize the original image and the translated image. To this end, we propose a content-aware consistency loss to guarantee translated data that do not lose the original image content, local pattern, and texture information.

3) Different From the Previous Feature-Level Adversarial Learning Algorithms [49], [50]: This directly learns the domain-invariant features; the proposed method is based on high-quality image translation, which is more interpretable. Besides, it can be treated as data augmentation. Cai *et al.* [56] proposed a two-stage domain adaptation method, which first utilizes adversarial learning in multilevel feature to strengthen target domain's adaptability and then uses the predicted density maps in the first stage as the pseudo labels to retrain the counter.

III. OUR METHOD

Here, the proposed DACC depicted in Fig. 2 is explained from the perspective of data flow. Specifically, a source domain provides crowd images $I_{\mathcal{S}}$ with the labeled density maps $A_{\mathcal{S}}$ and a target domain only provides images $I_{\mathcal{T}}$. The purpose is to get the prediction density maps $\hat{A}_{\mathcal{T}}$ according to given $I_{\mathcal{S}}$, $A_{\mathcal{S}}$, and $I_{\mathcal{T}}$. To help the reader understand, some of the symbols used behind are concluded in Table I.

A. High-Quality Image Translation for Crowd Counting

Image translation aims to translate source images $I_{\mathcal{S}}$ to like-target data $\hat{I}_{\mathcal{S}\text{to}\mathcal{T}}$. At the same time, the latter is supposed to contain the key crowd contents of the former. Inspired by the disentangled representation [51], [52], we propose an IFS framework to separate the crowd contents and domain-independent attributes. Finally, exploiting the translated images and source labels, we train a coarse crowd counter.

1) Interdomain Features Segregation: The following conditions hold.

a) Assumption: For crowd scenes of different domains, some essential contents are shared, such as the structure information of persons and the arrangement of congested crowds. Meanwhile, each domain has its private attributes, such as different backgrounds, image styles, and viewpoints. Thus, we assume that a source domain shares a latent feature space with any other target domain, and each domain has its independent attribute.

b) Model overview: Based on this assumption, the purpose of IFS is supposed to separate common crowd contents and private attributes without overlapping. It consists of two components: a domain-shared features extractor $\boldsymbol{G}_c$ and two domain-specific decoders $\boldsymbol{G}_{\text{to}\mathcal{S}}$ and $\boldsymbol{G}_{\text{to}\mathcal{T}}$ for source and target domains. To separate two types of features, we design three corresponding adversarial discriminators for them. The discriminators attempt to distinguish which domain the outputs of $\boldsymbol{G}_c$, $\boldsymbol{G}_{\text{to}\mathcal{S}}$, and $\boldsymbol{G}_{\text{to}\mathcal{T}}$ come from. By optimizing generators and discriminators in turns, $\boldsymbol{G}_c$ can extract domain-shared features, and $\boldsymbol{G}_{\text{to}\mathcal{S}}$ and $\boldsymbol{G}_{\text{to}\mathcal{T}}$ can reconstruct source domain-like or target domain-like crowd scenes according to the outputs of feature extractor. Consequently, the domain-shared features are extracted explicitly and the domain-specific features are implicitly contained in the source domain decoder and the target domain decoder.

c) Domain-shared features extractor $\boldsymbol{G}_c$: Based on the above assumption, it is important to ensure that feature extractor extracts similar feature distributions for the samples from different domains (namely, $i_{\mathcal{S}} \in I_{\mathcal{S}}$ and $i_{\mathcal{T}} \in I_{\mathcal{T}}$). To this end, we introduce feature-level adversarial learning for $f_{\mathcal{S}}$ and $f_{\mathcal{T}}$ produced by the features extractor, of which is corresponding to source domain and target domain, respectively. Specifically, training a discriminator $\boldsymbol{D}_c$ to distinguish whether the features come from source domain or target domain. At the same time, updating the parameters of feature extractor to fool $\boldsymbol{D}_c$ by using the loss of the inverse discrimination result. Consequently, $f_{\mathcal{S}}$ and $f_{\mathcal{T}}$ are very similar and share the same feature space.

d) Domain-specific decoders $\boldsymbol{G}_{to\mathcal{S}}$ and $\boldsymbol{G}_{to\mathcal{T}}$: The proposed $\boldsymbol{G}_c$ can extract the features that share the same feature space, but it does not mean that they are key contents mentioned in the assumption. Thus, we propose two domain-specific decoders for domain $\mathcal{S}$ and $\mathcal{T}$, which reconstructs images like own domain according to the outputs of feature extractor. On the one hand, this process encourages a feature extractor to extract effective domain-shared features. On the other hand, it makes $\boldsymbol{G}_{\text{to}\mathcal{S}}$ and $\boldsymbol{G}_{\text{to}\mathcal{T}}$ contain the domain-independent attributes.

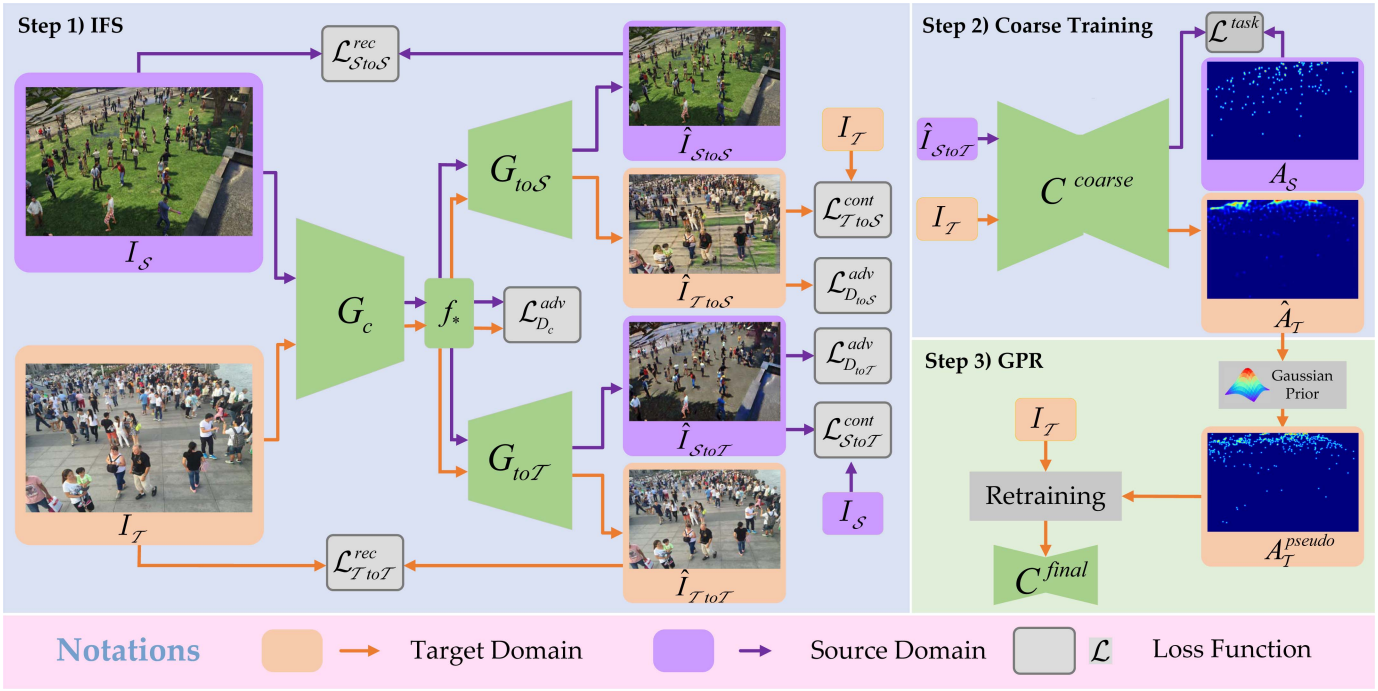

Fig. 2. Flowchart of our proposed method, which consists of three components: 1) IFS translates $I_{\mathcal{S}}$ to $I_{\mathcal{S}to\mathcal{T}}$; 2) train the coarse counter $\boldsymbol{C}^{\text{coarse}}$ using $I_{\mathcal{S}to\mathcal{T}}$ and $A_{\mathcal{S}}$; 3) after $\boldsymbol{C}^{\text{coarse}}$ converges via iteratively optimizing Steps 1) and 2), reconstruct the pseudo map $A_{\mathcal{T}}^{\text{pseudo}}$ from $\boldsymbol{C}^{\text{coarse}}$'s predictions $\hat{A}_{\mathcal{T}}$ and retrain the final counter $\boldsymbol{C}^{\text{final}}$ using $I_{\mathcal{T}}$ and $A_{\mathcal{T}}^{\text{pseudo}}$. Limited by this article space, the three discriminators are not shown in the figure.

To achieve the above goals, we introduce adversarial networks $\boldsymbol{D}_{\text{to}\mathcal{S}}$ and $\boldsymbol{D}_{\text{to}\mathcal{T}}$ for each domain-specific decoders. They attempt to determine which domain is the origin of reconstructed images. Taking $\{f_{\mathcal{S}}, f_{\mathcal{T}}, \boldsymbol{G}_{\text{to}\mathcal{T}}, \boldsymbol{D}_{\text{to}\mathcal{T}}\}$ as an example, feed $f_{\mathcal{S}}$ and $f_{\mathcal{T}}$ into $\boldsymbol{G}_{\text{to}\mathcal{T}}$, and then, attain $\hat{i}_{\mathcal{S}to\mathcal{T}}$ and $\hat{i}_{\mathcal{T}to\mathcal{T}}$, respectively. $\boldsymbol{D}_{\text{to}\mathcal{T}}$ aims to distinguish the domains of $\hat{i}_{\mathcal{S}to\mathcal{T}}$ and $\hat{i}_{\mathcal{T}}$. Similar to the above feature-level adversarial training, the loss of the inverse discrimination result is used to update $\boldsymbol{G}_c$ and $\boldsymbol{G}_{\text{to}\mathcal{T}}$. As a result, the photorealistic image $\hat{i}_{\mathcal{S}to\mathcal{T}}$ is generated to fool $\boldsymbol{D}_{\text{to}\mathcal{T}}$.

2) Coarse Training for Crowd Counting: After generating the translated images $\hat{I}_{\mathcal{S}to\mathcal{T}}$, the coarse counter $\boldsymbol{C}^{\text{coarse}}$ is trained on $\hat{I}_{\mathcal{S}to\mathcal{T}}$ and $A_{\mathcal{S}}$ by using the traditional supervising regression method. In practice, given a batch of translation results in each iteration of IFS, $\boldsymbol{C}^{\text{coarse}}$ will be trained once. In other word, the image translation model and the coarse counter are trained together.

3) Loss Functions: To train the proposed framework, in each iteration, the discriminators $\boldsymbol{D}_c$, $\boldsymbol{D}_{\text{to}\mathcal{S}}$, and $\boldsymbol{D}_{\text{to}\mathcal{T}}$ are updated using an adversarial loss; then, update the parameters of $\boldsymbol{G}_c$, $\boldsymbol{G}_{\text{to}\mathcal{S}}$, $\boldsymbol{G}_{\text{to}\mathcal{T}}$, and $\boldsymbol{C}^{\text{coarse}}$ by optimizing the following functions:

$$\mathcal{L} = \mathcal{L}^{\text{task}} + \alpha\mathcal{L}^{\text{adv}}_{\boldsymbol{D}_c} + \beta\mathcal{L}^{\text{adv}}_{\boldsymbol{D}_{\text{to}\mathcal{S}}} + \gamma\,\mathcal{L}^{\text{adv}}_{\boldsymbol{D}_{\text{to}\mathcal{T}}} + \mathcal{L}^{\text{cons}} \tag{1}$$

where the first item is task loss for counting, the middle threes are adversarial loss for three discriminators, and the last item is the consistency loss. By repeating the above training, the models will be obtained. Next, we will explain the concrete definitions of them. Note that θ_* means the parameters of the model $*$.

a) Task loss: For the counting task, we train $\boldsymbol{C}^{\text{coarse}}$ via optimizing $\mathcal{L}^{\text{task}}(\theta_{\boldsymbol{C}^{\text{coarse}}})$, a standard mean squared error (MSE) loss.

b) Feature-level adversarial loss: To effectively extract domain-shared features, we minimize a feature-level LSGAN loss [57] to train $\boldsymbol{D}_c$. The loss and inverse loss are denoted by $\mathcal{L}_{\boldsymbol{D}_c}$ and $\mathcal{L}^{\text{adv}}_{\boldsymbol{D}_c}$, respectively.

c) Multiscale translation adversarial loss: We find that the traditional methods are prone to generating weird data that contain distorted color distribution. The main reason is that the adversarial training is unstable and it causes that some neurons are sensitive to specific data. To alleviate this problem, we propose a multiscale translation adversarial loss (MS Ad), which adopts a full convolution discriminator to distinguish the domains of two images under the different image scales. It is an MSE-like loss and has been proven in LSGAN [57] with better stability compared with the cross-entropy loss. Taking $\boldsymbol{D}_{\text{to}\mathcal{S}}$ as an example, $\mathcal{L}_{\boldsymbol{D}_{\text{to}\mathcal{S}}}$ and $\mathcal{L}^{\text{adv}}_{\boldsymbol{D}_{\text{to}\mathcal{S}}}$ are formulated as

$$\mathcal{L}_{\boldsymbol{D}_{\text{to}\mathcal{S}}}(\theta_{\boldsymbol{D}_{\text{to}\mathcal{S}}}) = \frac{1}{2}\sum_{l=1}^{2}\left\{\left|\left|\boldsymbol{D}_{\text{to}\mathcal{S}}\left(i_{\mathcal{S}}^{l}\right) - 0\right|\right|^2 + \left|\left|\boldsymbol{D}_{\text{to}\mathcal{S}}\left(i_{\mathcal{T}\text{to}\mathcal{S}}^{l}\right) - 1\right|\right|^2\right\} \tag{2}$$

and

$$\mathcal{L}^{\text{adv}}_{\boldsymbol{D}_{\text{to}\mathcal{S}}}\left(\theta_{\boldsymbol{G}_c}, \theta_{\boldsymbol{G}_{\text{to}\mathcal{S}}}\right) = \frac{1}{2}\sum_{l=1}^{2}\left|\left|\boldsymbol{D}_{\text{to}\mathcal{S}}\left(i_{\mathcal{T}\text{to}\mathcal{S}}^{l}\right) - 0\right|\right|^2 \tag{3}$$

where $l = 1$ and 2, respectively, represent the size of inputs, namely, $0.5\times$ and $1.0\times$. During the training, $\boldsymbol{D}_{\text{to}\mathcal{S}}$ attempts

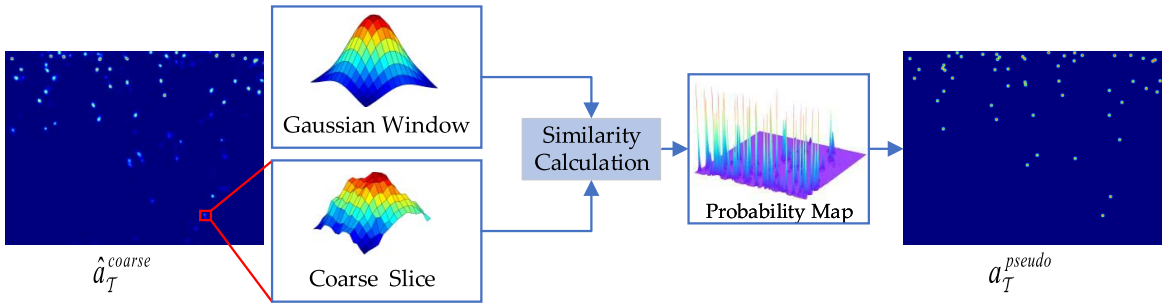

Fig. 3. Generation process of pseudo labels.

to distinguish the origins of $i_{\mathcal{S}}$ and $i_{\mathcal{T}\text{to}\mathcal{S}}$. At the same time, by optimizing $\mathcal{L}_{\boldsymbol{D}_{\text{to}\mathcal{S}}}^{\text{adv}}$, $\boldsymbol{G}_c$ and $\boldsymbol{G}_{\text{to}\mathcal{S}}$ are updated to generate like-target images that can confuse $\boldsymbol{D}_{\text{to}\mathcal{S}}$. Similarly, there are $\mathcal{L}_{\boldsymbol{D}_{\text{to}\mathcal{T}}}(\theta_{\boldsymbol{D}_{\text{to}\mathcal{T}}})$ and $\mathcal{L}_{\boldsymbol{D}_{\text{to}\mathcal{T}}}^{\text{adv}}(\theta_{\boldsymbol{G}_c}, \theta_{\boldsymbol{G}_{\text{to}\mathcal{T}}})$ to train $\boldsymbol{D}_{\text{to}\mathcal{S}}$ and $\{\boldsymbol{G}_c, \boldsymbol{G}_{\text{to}\mathcal{S}}\}$, respectively.

d) Consistency loss: The mainstream translation methods have two data flows: recall process ($i_{\mathcal{S}} \rightarrow \hat{i}_{\mathcal{S}\text{to}\mathcal{S}}$) and the translation process ($i_{\mathcal{T}} \rightarrow \hat{i}_{\mathcal{T}\text{to}\mathcal{S}}$). For the former, the researchers [18] usually regularize the data using pixelwise consistency loss (namely, L2 loss). However, for image translation task, the ultimate goal is translating images instead of recalling images. Many works ignore the latter so that the model loses the original content and detailed features.

To remedy this problem, we attempt to design a loss function to constrain high-level image content. The L2 loss in recall process is improper because it only measures the pixelwise distance, which is antitranslation operation. Therefore, we propose a content-aware consistency loss to regularize $i_{\mathcal{T}}$ and $\hat{i}_{\mathcal{T}\text{to}\mathcal{S}}$. To be specific, we adopt perceptual losses [58] to formulate the difference of feature maps extracted by a pretrained classification model VGG-16 [59], which are named $\mathcal{L}_{\mathcal{T}\text{to}\mathcal{S}}^{\text{cont}}(\theta_{\boldsymbol{G}_c}, \theta_{\boldsymbol{G}_{\text{to}\mathcal{S}}})$ and $\mathcal{L}_{\mathcal{S}\text{to}\mathcal{S}}^{\text{cont}}(\theta_{\boldsymbol{G}_c}, \theta_{\boldsymbol{G}_{\text{to}\mathcal{S}}})$. It effectively maintains low-level local features and high-level crowd contents of the original image. Similarly, there are $\mathcal{L}_{\mathcal{T}\text{to}\mathcal{T}}^{\text{rec}}(\theta_{\boldsymbol{G}_c}, \theta_{\boldsymbol{G}_{\text{to}\mathcal{T}}})$ and $\mathcal{L}_{\mathcal{S}\text{to}\mathcal{T}}^{\text{cont}}(\theta_{\boldsymbol{G}_c}, \theta_{\boldsymbol{G}_{\text{to}\mathcal{T}}})$ to regularize the outputs of $\boldsymbol{G}_{\text{to}\mathcal{T}}$.

Finally, $\mathcal{L}^{\text{cons}}$ in (1) is the sum of the above four consistency losses.

B. Gaussian-Prior Reconstruction

In the field of crowd counting, the ground truth of density map is generated using head locations and Gaussian kernel [25]. The goal of Gaussian-prior reconstruction (GPR) is to find the most likely head locations via comparing the coarse map and the standard kernel. After this, the pseudo map is reconstructed and used to train a final counter on the target domain.

1) Density Map Generation: First, we briefly review the generation process of density maps in traditional supervised methods. In the field of counting, the original label form is a set of heads positions $(\boldsymbol{x}, \boldsymbol{y}) = \{(x_1, y_1), \ldots, (x_N, y_N)\}$. Taking a sample (x_i, y_i) as an example, it is treated as a delta function $\delta(x - x_i, y - y_i)$. Therefore, the position set can be formulated as

$$H(\boldsymbol{x}, \boldsymbol{y}) = \sum_{i=1}^{N} \delta(x - x_i, y - y_i). \tag{4}$$

For getting the density map, we convolve $H(\boldsymbol{x}, \boldsymbol{y})$ with a Gaussian function $G_{k,\sigma}$, where k is the kernel size and σ is the standard deviation. In practice, $G_{k,\sigma}$ is regarded as a discrete Gaussian window $W_{k,\sigma}$ with the size of $k \times k$. To be specific, the value of position (u, v) in $W_{k,\sigma}$ is defined as $w(u, v) = e^{-D^2(u,v)/2\sigma^2}$, where $D(u, v)$ is the distance from (u, v) to the window center. It is defined as

$$D(u, v) = \left[((u - (k+1)/2)^2 + (v - (k+1)/2)^2\right]^{1/2}. \tag{5}$$

In the experiments, we set k as 15 and σ as 4.

2) Density Map Reconstruction: A standard map is recalled according to the coarse result $\hat{a}_{\mathcal{T}}$. It consists of three steps: 1) compute probability map at the pixel level, of which each pixel represents its confidence as a Gaussian kernel's center; 2) iteratively select a maximum probability candidate point and update the probability map in turns; and 3) generate pseudo labels based on candidate points.

Here, we detailedly explain the generation of the probability map. Take a pixel (x_i, y_i) in $\hat{A}_{\mathcal{T}}$ as the center, cropping a window $\hat{A}_{\mathcal{T}}^{(x_i,y_i)}$ with the size of $k \times k$ and then measuring the similarity between $\hat{A}_{\mathcal{T}}^{(x_i,y_i)}$ and $W_{k,\sigma}$ using the following formulation:

$$P(x_i, y_i) = \frac{1}{1 + \|\hat{A}_{\mathcal{T}}^{(x_i,y_i)} - W_{k,\sigma}\|_1} \tag{6}$$

where $W_{k,\sigma}$ is a discrete Gaussian window with the size of $k \times k$, $P(x_i, y_i) \in [0, 1]$ and the higher value means that it is closer to $W_{k,\sigma}$. Finally, the probability map P is obtained. The generation flow is shown in Fig. 3, and the computation process is demonstrated in Algorithm 1.

3) Retraining Scheme: Although the above reconstruction can effectively prompt the density quality, it may generate a few mistaken head labels from the coarse map. In addition, its time complexity is $O(n)$, which is not efficient. To remedy these problems, we retrain a final counter $\boldsymbol{C}^{\text{final}}$ using $I_{\mathcal{T}}$ and $A_{\mathcal{T}}^{\text{pseudo}}$ based on the $\theta_{\boldsymbol{C}^{\text{coarse}}}$. The error labels will be alleviated as the model converges. During the test phase, $\boldsymbol{C}^{\text{final}}$ is performed to direct more high-quality predictions than the coarse results.

C. Network Architecture

This section briefly describes our network architectures. $\boldsymbol{G}_c$ consists of four residual blocks and outputs a 512-channel feature map with the 1/4 size of inputs. $\boldsymbol{G}_{\text{to}\mathcal{S}}$ and $\boldsymbol{G}_{\text{to}\mathcal{T}}$ have the same architecture, including six convolutional/deconvolutional layers. For the discriminators, they are all designed as

Algorithm 1 Algorithm for Generating Pseudo Labels

Require: Coarse map $\hat{A}_{\mathcal{T}}$, Gaussian Window $W_{k,\sigma}$.
Ensure: Pseudo label map $A_{\mathcal{T}}^{pseudo}$.
1: Count the number of people, $\hat{N} = int(sum(\hat{A}_{\mathcal{T}}))$;
2: Compute the probability map P for $\hat{A}_{\mathcal{T}}^{coarse}$ with Eq. 6;
3: **for** $j = 1$ to $\hat{N}$ **do**
4: Get a candidate point $(\hat{x}_j, \hat{y}_j) = \arg\max_{(\hat{x}_j,\hat{y}_j)}(P(\hat{x}_j, \hat{y}_j))$;
5: Crop a window $\hat{A}_{\mathcal{T}}^{(\hat{x}_j,\hat{y}_j)}$ with the center $(\hat{x}_j,\hat{y}_j)$ from $\hat{A}_{\mathcal{T}}$;
6: Update $\hat{A}_{\mathcal{T}}^{(\hat{x}_j,\hat{y}_j)} = \hat{A}_{\mathcal{T}}^{(\hat{x}_j,\hat{y}_j)} - W_{k,\sigma}$;
7: Place $\hat{A}_{\mathcal{T}}^{(\hat{x}_j,\hat{y}_j)}$ back to $\hat{A}_{\mathcal{T}}$;
8: Recompute P's region where changes occur in $\hat{A}_{\mathcal{T}}$;
9: **end for**
10: Generate the map $A_{\mathcal{T}}^{pseudo}$ with $\{(\hat{x}_1, \hat{y}_1), \ldots, (\hat{x}_{\hat{N}}, \hat{y}_{\hat{N}})\}$.
11: **return** $A_{\mathcal{T}}^{pseudo}$.

a five-layer convolution network. The counters utilize the first ten layers of VGG-16 [59] and upsample to the original size via a series of deconvolutional layers. All detailed configurations of the networks are shown in the Supplementary Materials, and the code will be released as soon as possible.

D. Implementation Details

1) Parameter Setting: During the training process of IFS, the weight parameters α, β, and γ in (1) are set to 0.01, 0.1, and 0.1, respectively. Due to the limited memory, in each iteration, we input four source images and four target images with a crop size of 480×480. The Adam algorithm [60] is performed to optimize the networks. The learning rate for the IFS models is set as 10^{-4}, and the learning rate for $\boldsymbol{C}^{\text{coarse}}$ is initialized as 10^{-5}. After 4000 iterations, we stop updating the IFS models, but continue to update $\boldsymbol{C}^{\text{coarse}}$ until it converges. For GPR process, $\boldsymbol{C}^{\text{final}}$'s learning rate is set as 10^{-5}. Our code is developed based on the C^3 framework [61] on NVIDIA GTX 1080Ti GPU.

2) Scene Regularization: In other fields of domain adaptation, such as semantic segmentation, the object distribution in street scenes is highly consistent. Unlike this, current crowd real-world datasets are very different in terms of density. For avoiding negative adaptation, we adopt a scene regularization strategy proposed in [17]. In other word, we manually select some proper synthetic scenes from GCC as the source domain for different target domains. Due to no experiment on UCSD [62] and Mall [63] in SE CycleGAN [17], we define the scene regularization for them. The detailed information is shown in the Supplementary Material.

IV. Experimental Results

A. Evaluation Criteria

Following the convention, we utilize a mean absolute error (MAE) and MSE to measure the counting performance of models, which are defined as

$$\text{MAE} = \frac{1}{N}\sum_{i=1}^{N}|y_i - \hat{y}_i|, \quad \text{MSE} = \sqrt{\frac{1}{N}\sum_{i=1}^{N}|y_i - \hat{y}_i|^2} \quad (7)$$

where N is the number of images, y_i is the ground truth number of people, and $\hat{y}_i$ is the estimated value for the ith image. Besides, peak signal to noise ratio (PSNR) and structural similarity (SSIM) [64] are adopted to evaluate the quality of density maps.

TABLE II
Performance of the Proposed Different Models on Shanghai Tech Part A

Method	Shanghai Tech Part A			
	MAE	MSE	PSNR	SSIM
NoAdpt	206.7	297.1	18.64	0.335
IFS-a	127.3	190.6	21.80	0.458
IFS-b	120.8	184.6	21.41	0.466
IFS-b + GPR-a	120.6	184.4	19.73	**0.760**
IFS-b + GPR-b (DACC)	**112.4**	**176.9**	**21.94**	0.502

B. Datasets

For verifying the proposed domain-adaptive method, the experiments are conducted from GCC [17] to another six real-world ones, namely, Shanghai Tech Part A/B [27], UCF-QNRF [33], WorldExpo'10 [65], Mall [62], and UCSD [63].

GCC is a large-scale synthetic dataset, which consists of still 15 212 images with a resolution of 1080×1920.

Shanghai Tech Part A is a congested crowd dataset, of which images are from a photosharing website. It consists of 482 images with different resolutions.

Shanghai Tech Part B is captured from the surveillance camera on the Nanjing Road in Shanghai, China. It contains 716 samples with a resolution of 768×1024.

UCF-QNRF is an extremely congested crowd dataset, including 1535 images collected from the Internet and annotating in 1 251 642 instances.

WorldExpo'10 is collected from 108 surveillance cameras in Shanghai 2010 WorldExpo, which contains 3980 images with a size of 576×720.

Mall is collected using a surveillance camera installed in a shopping mall, which records the 2000 sequential frames with a resolution of 480×640.

UCSD is an outdoor single-scene dataset collected from a video camera at a pedestrian walkway, which contains 2000 image sequences with a size of 158×238.

C. Module-Level Ablation Study on Shanghai Tech Part A

We conduct a group of detailed ablation study to verify the effectiveness of our proposed models on Shanghai Tech Part A. To be specific, the different models' configurations are explained as follows.

Table II reports the quantitative results of different module fusion methods.

NoAdpt: Train the counter on the original GCC.

IFS-a: Train the translated GCC of IFS w/o feature-level adversarial learning.

IFS-b: Train the translated GCC of IFS with feature-level adversarial learning.

IFS-b + GPR-a: Reconstruct pseudo labels using the results of the counter in IFS-b.

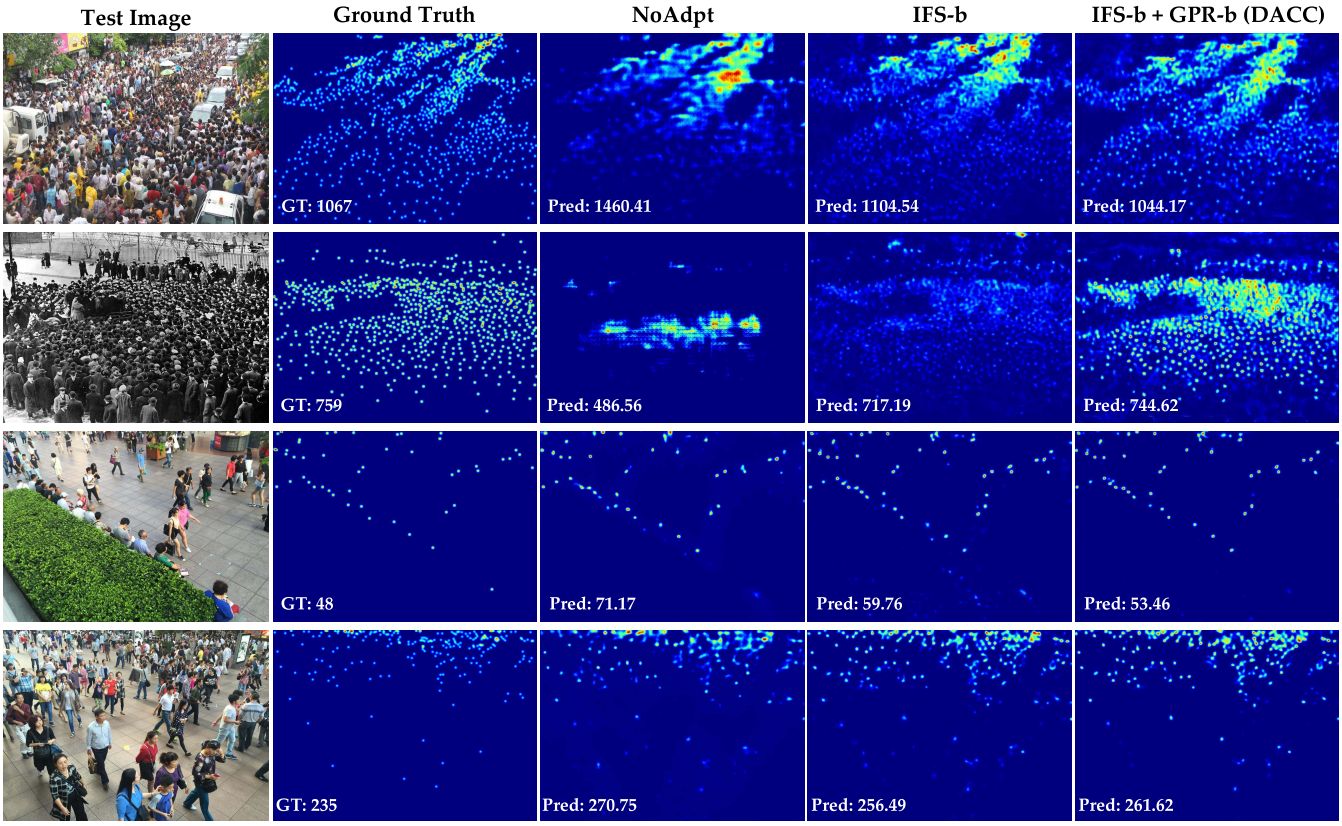

Fig. 4. Exemplar results of adaptation from GCC to Shanghai Tech Part A and B dataset. In the density map. "GT" and "Pred" represent the number of ground truth and prediction, respectively. Rows 1 and 2 come from ShanghaiTech Part A, and others are from Part B.

IFS-b + GPR-b: Retrain the counter with the pseudo labels of IFS-b + GPR-a. It is the full model of this article, namely, the proposed DACC.

Analysis of IFS: From the table, the methods with adaptation far exceed NoAdpt, which shows the effectiveness of domain adaptation. By comparing the results IFS-a and IFS-b, the errors are significantly reduced (MAE/MSE: from 127.3/190.6 to 120.8/184.6). It indicates that feature-level adversarial learning effectively facilitates the segregation of interdomain features.

Analysis of GPR: When introducing GPR-a into IFS-b, the counting errors are slightly different (MAE/MSE: 120.8/184.6 versus 120.6/184.4). The main reason is the rounding operation for counting number in Line 1 of Algorithm 1. It is a double-edged sword, which may be decreased or increased the errors. The slight performance fluctuations are not important. Our concern is to improve the quality of density map and remove some misestimations by the further retraining scheme. Correspondingly, since GPR-a generates the standard pseudo labels, SSIM achieves the value of 0.760, far more than the previous result of 0.466. After retraining a final counter, the mistaken estimations in the background are dramatically suppressed. As a result, the MAE and MSE of DACC are further reduced (MAE/MSE: 120.6/184.4 versus 112.4/176.9).

Visualization Results: Fig. 4 shows the visualization results of the proposed stepwise models (NoAdpt, IFS-b, and IFS-b + GPR-b) on Shanghai Tech Part A and B. From the results of Column 3, NoAdpt only reflects the trend of density distribution. For the second sample, NoAdpt produces a weird density map, which seems to be not consistent with the original image. The main reason is that GCC data are RGB images, but the second sample is a grayscale scene. The NoAdpt counter fully overfits the RGB data so that it performs poorly on grayscale images. After introducing IFS, the visual results can show the coarse density distribution. For some sparse crowd regions (such as Row 3), the counter yields the fine density map close to the ground truth. Furthermore, the final results of DACC present two advantages in visual perception. First, DACC outputs the more precise density maps, of which points are similar to the standard Gaussian kernel. It will prompt the performance of person localization. Second, the mistaken estimations are effectively reduced, especially in Rows 3 and 4. In general, DACC's predictions are better than those of other models in terms of quantitative and qualitative comparisons.

D. Loss-Level Ablation Study on UCF-QNRF

In Section I, we mentioned that our losses can significantly maintain the local patterns and texture features, especially for dense crowd. Here, we will verify our opinion by using the experiments that use different translation models (CycleGAN and our IFS-b) on the most congested dataset: UCF-QNRF. The results are reported in Table III. Here, we describe the

TABLE III
PERFORMANCE OF THE PROPOSED DIFFERENT LOSS COMBINATIONS ON UCF-QNRF

Loss Combinations	CycleGAN Structure				IFS-b Structure			
	MAE	MSE	PSNR	SSIM	MAE	MSE	PSNR	SSIM
Ad + C (original)	257.3	400.6	20.80	0.480	243.9	392.6	20.77	0.607
MS Ad + C	232.9	394.0	20.97	0.575	221.8	385.9	21.23	0.642
ad + c + SE	230.4	384.5	21.03	**0.660**	225.3	281.7	21.57	**0.690**
ad + c + CA	223.7	381.7	21.09	0.612	215.8	361.0	21.77	0.676
MS Ad + C + CA	**218.1**	**380.0**	**21.17**	0.624	**211.7**	**357.9**	**21.94**	0.687

TABLE IV
PERFORMANCE OF NO ADAPTATION (NO ADPT), CYCLEGAN, SE CYCLEGAN, FSC, FA, AND THE PROPOSED METHODS ON THE SIX REAL-WORLD DATASETS

Method	DA	Shanghai Tech Part A				Shanghai Tech Part B				UCF-QNRF			
		MAE	MSE	PSNR	SSIM	MAE	MSE	PSNR	SSIM	MAE	MSE	PSNR	SSIM
CycleGAN [18]	✔	143.3	204.3	19.27	0.379	25.4	39.7	24.60	0.763	257.3	400.6	20.80	0.480
SE CycleGAN [17]	✔	123.4	193.4	18.61	0.407	19.9	28.3	24.78	0.765	230.4	384.5	21.03	0.660
SE Cycle GAN (JT) [66]	✔	119.6	189.1	18.69	0.429	16.4	25.8	26.17	0.786	225.9	385.7	21.10	0.642
FSC [49]	✔	129.3	187.6	21.58	**0.513**	16.9	24.7	26.20	0.818	221.2	390.2	**23.10**	0.708
FA [50]	✔	144.6	200.6	-	-	16.0	24.7	-	-	269.5	407.9	-	-
LIDK [56]	✔	-	-	-	-	14.3	22.8	-	-	224.3	375.8	-	-
NoAdpt (ours)	✗	206.7	297.1	18.64	0.335	24.8	34.7	25.02	0.722	292.6	450.7	20.83	0.565
DACC (ours)	✔	**112.4**	**176.9**	**21.94**	0.502	**13.1**	**19.4**	**28.03**	**0.888**	**203.5**	**343.0**	21.99	**0.717**

Method	DA	WorldExpo'10 (only MAE)						UCSD				Mall			
		S1	S2	S3	S4	S5	Avg.	MAE	MSE	PSNR	SSIM	MAE	MSE	PSNR	SSIM
CycleGAN [18]	✔	4.4	69.6	49.9	29.2	9.0	32.4	-	-	-	-	-	-	-	-
SE CycleGAN [17]	✔	**4.3**	59.1	43.7	17.0	7.6	26.3	-	-	-	-	-	-	-	-
SE Cycle GAN (JT) [66]	✔	**4.2**	**49.6**	**41.3**	19.8	**7.2**	**24.4**	-	-	-	-	-	-	-	-
FA [50]	✔	5.7	59.9	19.7	**14.5**	8.1	21.6	2.00	2.43	-	-	2.47	3.25	-	-
NoAdpt (ours)	✗	11.0	49.2	72.2	40.2	17.2	38.0	14.95	15.31	23.66	0.909	5.92	6.70	25.02	0.886
DACC (ours)	✔	4.5	**33.6**	**14.1**	30.4	**4.4**	**17.4**	**1.76**	**2.09**	**24.42**	**0.950**	**2.31**	**2.96**	**25.54**	**0.933**

notations in the table: "Ad" means the traditional adversarial loss used by CycleGAN, and "C" indicates the standard consistency loss used by CycleGAN [18]. SE is SSIM embedding loss proposed by SE CycleGAN [17]. "MS Ad" and "CA" are our designed multiscale adversarial loss and context-aware consistency loss, respectively.

By comparing the results of the two translation structures, we find that the proposed IFS-b is better than CycleGAN under the same training loss combination. The former can extract more effective domain-invariant features than the latter. It evidences that two-stage translation via segregating domain-shared and domain-independent features can generate more similar data to real scenes. In Section V-A and Fig. 5, we discuss the translation quality of these two structures.

1) Ad Loss Versus MS Ad Loss: Different from the previous methods, we attempt to regularize translated images at two resolutions, which facilitates the generator's neurons more robust and remedies the distortion translation outputs. From the final counting errors (MAE), the MS Ad loss has 9.5% (Cycle GAN structure) and 9.1% (IFS-b structure) improvements than the traditional Ad Loss.

2) CA Loss Versus C Loss: C loss only aims at the recall quality, which does not directly affect the translation. After introducing the CA loss, the translation quality is prompted and the model attains a better counting performance (13.1% and 11.5% improvements of MAE on Cycle GAN and IFS-b structure).

3) SE Loss Versus CA Loss: Both focus on improving the translation quality on congested regions. By the comparison of the reported results, we find that the CA loss is superior to the SE loss in terms of counting performance. From the perspective of translation quality, SE loss has a more significant effect than CA loss (0.660 versus 0.612). The main reason is that the SE loss mainly focuses on local structural similarity instead of high-level image contents.

E. Comparison With the SOTAs on Real-World Datasets

In this section, we perform the experiments of DACC on six mainstream real-world datasets and compare the performance with other domain-adaptive counting methods, such as CycleGAN [18], SE CycleGAN [17], FSC [49], FA [50], and LIDK [56]. Table IV lists the concrete four

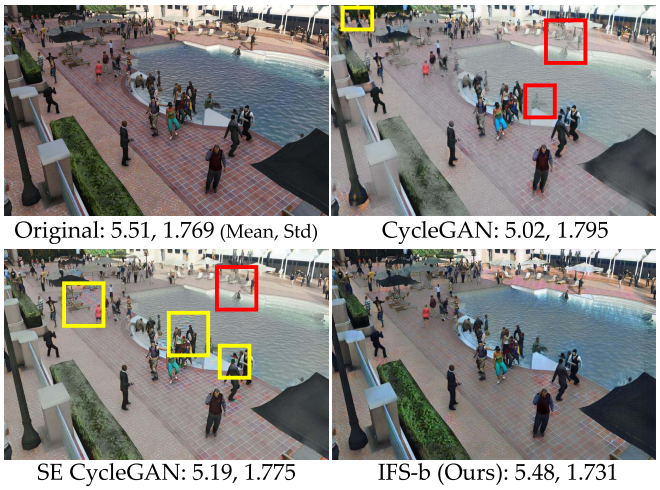

Fig. 5. Comparisons of the adaptation on GCC → ShanghaiTech Part B.

metrics (MAE↓/MSE↓/PSNR↑/SSIM↑). From it, the proposed DACC outperforms the other methods on all datasets. Taking MAE as an example, DACC achieves 112.4, 13.1, 203.5, 17.4, 1.76, and 2.31 on the six real-world datasets. In terms of some results on density quality, FSC is better than ours. The main reason is that FSC uses the crowd mask to align the semantic consistency. The extra label effectively reduces the estimation error in the background regions. More visualization results on other datasets are shown in the Supplementary Material.

Compared with NoAdpt, DACC significantly reduces the counting errors. Taking MAE as an example, DACC reduces the estimation errors by 45.7%, 47.2%, and 30.5% on the first three dense datasets. On the sparse WorldExpo'10, UCSD, and Mall datasets, DACC achieves more than 50% improvement, 54.2%, 88.2%, and 61.0%, respectively.

For the results on UCSD, we find that the PSNR and SSIM of density map are not good. The main reason is that the label definitions of them are different. The source domain (GCC) annotates the head position, but the target domain (UCSD) annotates the center position. Nevertheless, it does not affect the evaluation for counting the number of people.

V. Discussion

A. Analysis of Translated Image Quality With SOTAs

This section compares the translation results by visualization and image quality. Fig. 5 shows the three results of CycleGAN, SE CycleGAN, and our IFS-b. For the first two methods, they lose the key content and some detailed information, especially in the region red boxes. In addition, they also yield some distorted regions in yellow boxes. In general, IFS-b maintains the crowd content well.

As we all know, evaluating the translation closeness to the target domain is difficult because there is no reference image. Thus, we only assess the translation data from the perspective of image quality. Specifically, we utilize a neural image assessment (NIMA) [67], which rates images with a mean score and a standard deviation ("std" for short). Table V reports these two metrics of CycleGAN, SE CycleGAN, and the proposed IFS-b on GCC → ShanghaiTech B. We find that DACC is better than other translation methods. We also show the NoAdpt results, of which images are the original synthetic GCC data. From the scores of single image in Fig. 5, IFS-b also outperforms CycleGAN-style methods.

TABLE V
Quality Comparison of the Translated Images

Methods	Mean ↑	Std ↓
NoAdpt	5.467	1.757
CycleGAN	4.935	1.848
SE CycleGAN	5.041	1.846
DACC(ours)	**5.244**	**1.810**

TABLE VI
Performance of the Exchange Experiments (MAE/MSE)

Data flow: GCC→Mall	Data flow: UCSD→Mall
EXP1: 2.31/2.96	EXP2: 2.85/3.55
EXP1': 2.21/2.85	EXP2': 2.97/3.76

B. Visual Analysis of Task Performance With SOTA

To vividly show the effectiveness of DACC, we compare the visual results with the SE CycleGAN [17]. It is emphasized that SE CycleGAN [17] provides visualizations of its counting results on Shanghai Tech Part A and Shanghai Tech Part B. Thus, it can be gained directly and compared with the proposed DACC's counting results. Fig. 6 shows the task performance on Shanghai Tech Part A dataset with two methods, which shows that the density maps predicted by DACC are highly similar to the ground truth, while SE CycleGAN outputs very coarse density maps. This comparison illustrates that the proposed DACC is better than SE CycleGAN in both quality and accuracy.

C. Effectiveness of IFS

In Section III-A1, it is mentioned that IFS can effectively separate domain-shared and domain-independent features. Here, we evidence this thought by two groups of exchange experiments. To be specific, select two adaptations with the same target domain, and then, fix the data and exchange IFS models to translate images. Take two experiments as examples: 1) EXP1: GCC → Mall and 2) EXP2: UCSD → Mall. We hope to translate the GCC data in EXP1 to like-Mall images using the IFS models of EXP2. Then, get the final counter by the translated images and GPR. Finally, the evaluation is conducted on the target data, namely, Mall. The above experiment is defined as EXP1'. Also, the other exchange way is named EXP2' and vice versa.

The counting results are listed in Table VI, and the translation exemplars are shown in Fig. 7. From them, we find that given source and target data, exchanging IFS models barely affects the performance of crowd counting and image translation.

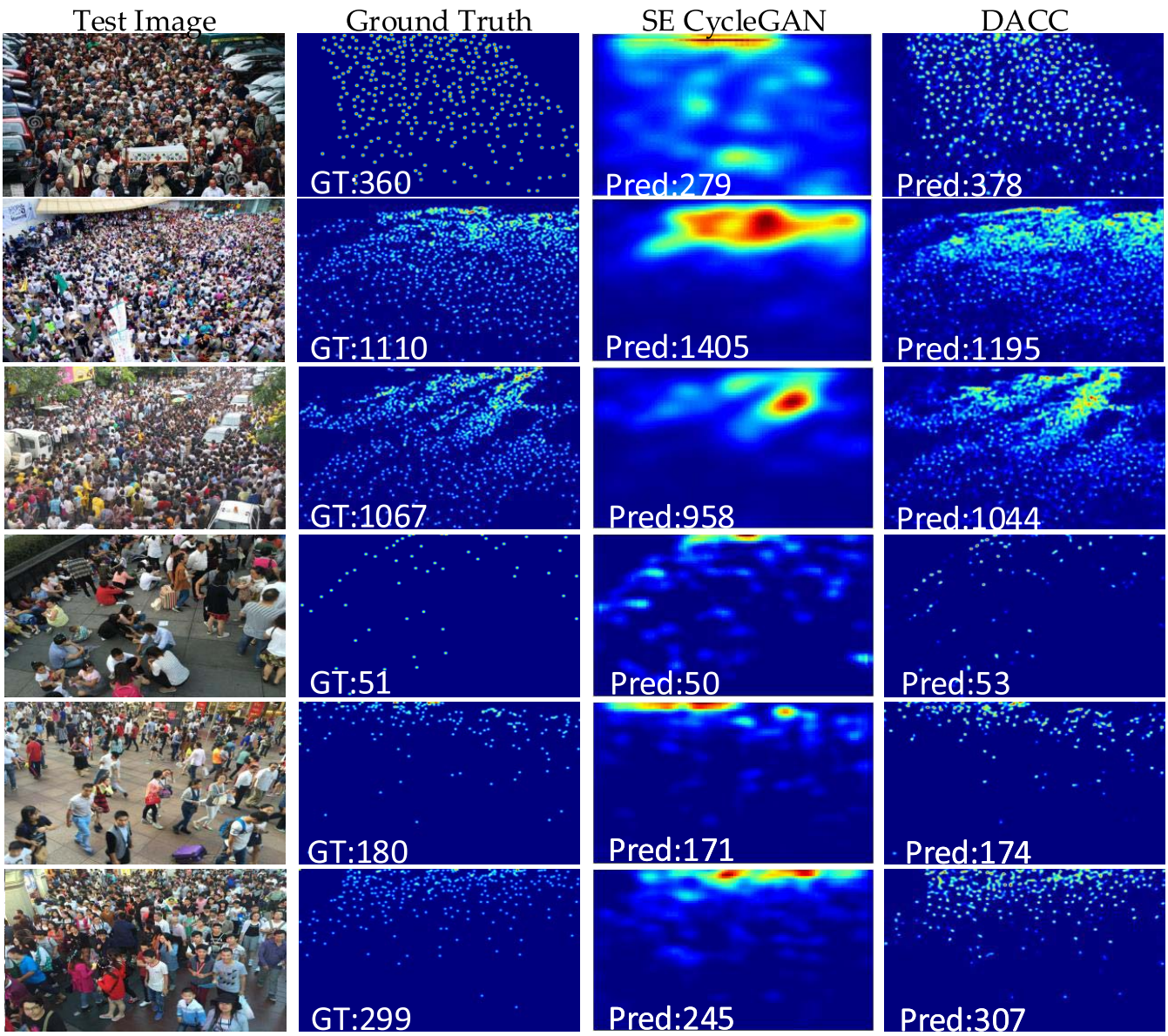

Fig. 6. Exemplar results of adaptation from GCC to Shanghai Tech Part A and B dataset. In the density map. "GT" and "Pred" represent the number of ground truth and prediction, respectively. Rows 1 and 2 come from ShanghaiTech Part A, and others are from Part B.

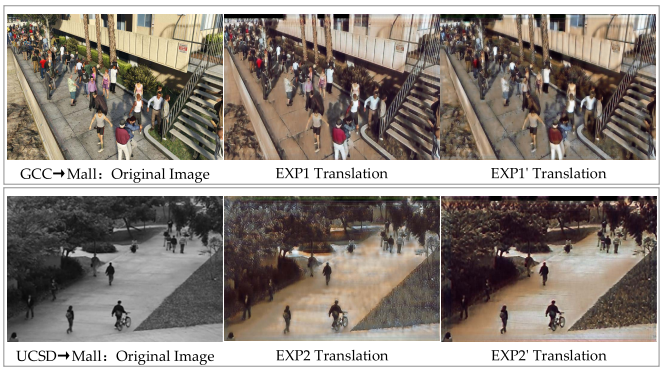

Fig. 7. Visual comparison of the model exchange experiments.

D. Performance of Counter C via Supervised Learning

In our work, the core is not to design a crowd counter, so we do not pay much attention to the supervised performance in the target domain. However, in order to prove that the IFS image translation proposed in this article can effectively reduce the domain gap, we conduct supervised training on several target domains. Table VII compares the performance of counter C between the supervised training in the target domain and domain adaptation. As shown in Table VII, the MAE and MSE of the counter used in this article are 69.6 and 125.9,

TABLE VII
COMPARISON OF C IN THE PROPOSED ADAPTATION METHOD AND SUPERVISED TRAINING

Methods	DA	T-GT	SHT A		SHT B	
			MAE	MSE	MAE	MSE
NoAdapt	✗	✗	206.7	297.1	24.8	34.7
DACC(ours)	✔	✗	112.4	176.9	13.1	19.4
Supervised	✗	✔	**69.6**	**125.9**	**8.1**	**14.1**

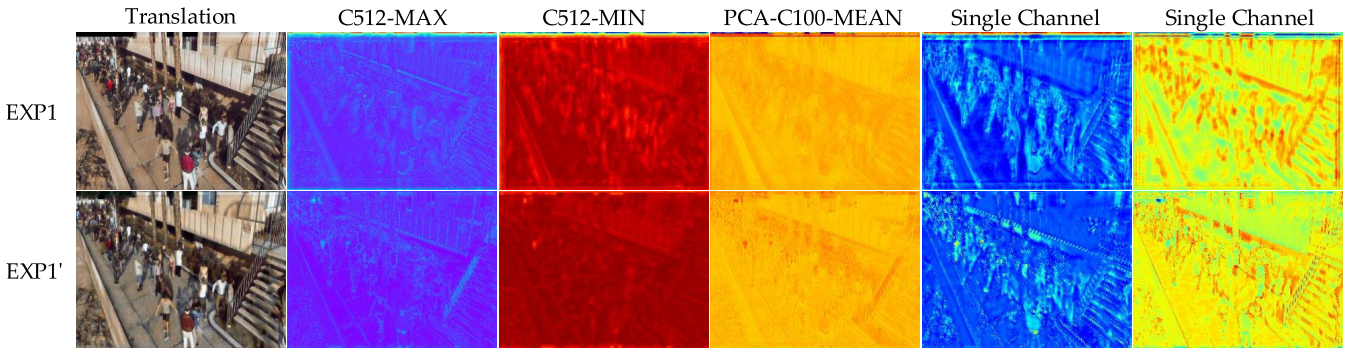

Fig. 8. Feature visualization of $\boldsymbol{G}_c$ in EXP1 and EXP1' with the same source image.

respectively, on Shanghai Tech Part A, and the MAE and MSE of supervised training on Shanghai Tech Part B are 8.1 and 14.1, respectively. The results in the table show that there is a large gap between no domain adaptation and supervised training, which is significantly reduced after domain adaptation.

E. IFS-b Domain-Shared Feature Visualization

In order to verify the effectiveness of our proposed IFS, we conduct a group of exchange experiments in Section IV-E. Here, we show the visualization results at the feature level. To be specific, the domain-shared features of $\boldsymbol{G}_c$ in EXP1 and EXP1' are shown in Fig. 8. The first column denotes the image translation results, and the second and third columns, respectively, represent the maximum and minimum values of each pixel in 512 channels. The fourth column is the average value of each pixel after reducing the original features to 100 channels via PCA. The last two are some similar features selected from 512-channel feature maps. From these visualization results, we find that different $\boldsymbol{G}_c$ from EXP1 and EXP1' can extract similar features for the same image. From Columns 5 and 6, there are high responses for the crowd region. In a word, these results evidence that the proposed IFS can extract domain-shared crowd contents.

VI. Conclusion

In this article, we present a DACC approach without any manual label. First, DACC translates synthetic data to high-quality photorealistic images by the proposed IFS. At the same time, we train a coarse counter on translated images. Then, GPR generates the pseudo labels according to the coarse results. By the retraining scheme, a final counter is obtained, which further refines the quality of density maps on real data. Experimental results demonstrate that the proposed DACC outperforms other state-of-the-art methods for the same task. In future work, we plan to extend IFS on multiple domains so that it can extract more effective and robust crowd contents to improve the counting performance.

References

[1] Q. Wang, M. Chen, F. Nie, and X. Li, "Detecting coherent groups in crowd scenes by multiview clustering," *IEEE Trans. Pattern Anal. Mach. Intell.*, vol. 42, no. 1, pp. 46–58, Jan. 2020.

[2] X. Li, M. Chen, F. Nie, and Q. Wang, "A multiview-based parameter free framework for group detection," in *Proc. 31st AAAI Conf. Artif. Intell.*, 2017, pp. 4147–4153.

[3] X. Li, M. Chen, F. Nie, and Q. Wang, "Locality adaptive discriminant analysis," in *Proc. 26th Int. Joint Conf. Artif. Intell.*, Aug. 2017, pp. 2201–2207.

[4] K. Kang and X. Wang, "Fully convolutional neural networks for crowd segmentation," 2014, *arXiv:1411.4464*.

[5] B. Zhou, X. Tang, and X. Wang, "Measuring crowd collectiveness," in *Proc. IEEE Conf. Comput. Vis. Pattern Recognit.*, Jun. 2013, pp. 3049–3056.

[6] K. Muhammad, J. Ahmad, Z. Lv, P. Bellavista, P. Yang, and S. W. Baik, "Efficient deep CNN-based fire detection and localization in video surveillance applications," *IEEE Trans. Syst., Man, Cybern., Syst.*, vol. 49, no. 7, pp. 1419–1434, Jul. 2018.

[7] B. Zhao, X. Li, and X. Lu, "HSA-RNN: Hierarchical structure-adaptive RNN for video summarization," in *Proc. IEEE/CVF Conf. Comput. Vis. Pattern Recognit.*, Jun. 2018, pp. 7405–7414.

[8] B. Zhao, X. Li, and X. Lu, "Property-constrained dual learning for video summarization," *IEEE Trans. Neural Netw. Learn. Syst.*, vol. 31, no. 10, pp. 3989–4000, Oct. 2020.

[9] Y. Yuan, Y. Feng, and X. Lu, "Structured dictionary learning for abnormal event detection in crowded scenes," *Pattern Recognit.*, vol. 73, pp. 99–110, Jan. 2018.

[10] C. Zhang, H. Li, X. Wang, and X. Yang, "Cross-scene crowd counting via deep convolutional neural networks," in *Proc. IEEE Conf. Comput. Vis. Pattern Recognit. (CVPR)*, Jun. 2015, pp. 833–841.

[11] D. B. Sam, S. Surya, and R. V. Babu, "Switching convolutional neural network for crowd counting," in *Proc. IEEE Conf. Comput. Vis. Pattern Recognit. (CVPR)*, Jul. 2017, pp. 4031–4039.

[12] D. B. Sam, N. N. Sajjan, R. V. Babu, and M. Srinivasan, "Divide and grow: Capturing huge diversity in crowd images with incrementally growing CNN," in *Proc. IEEE/CVF Conf. Comput. Vis. Pattern Recognit.*, Jun. 2018, pp. 3618–3626.

[13] J. Liu, C. Gao, D. Meng, and A. G. Hauptmann, "DecideNet: Counting varying density crowds through attention guided detection and density estimation," in *Proc. IEEE Conf. Comput. Vis. Pattern Recognit.*, Jun. 2018, pp. 5197–5206.

[14] Y. Li, X. Zhang, and D. Chen, "CSRNet: Dilated convolutional neural networks for understanding the highly congested scenes," in *Proc. IEEE/CVF Conf. Comput. Vis. Pattern Recognit.*, Jun. 2018, pp. 1091–1100.

[15] M. Shi, Z. Yang, C. Xu, and Q. Chen, "Revisiting perspective information for efficient crowd counting," in *Proc. IEEE/CVF Conf. Comput. Vis. Pattern Recognit. (CVPR)*, Jun. 2019, pp. 7279–7288.

[16] Q. Wang, J. Gao, W. Lin, and X. Li, "NWPU-crowd: A large-scale benchmark for crowd counting and localization," *IEEE Trans. Pattern Anal. Mach. Intell.*, vol. 43, no. 6, pp. 2141–2149, Jun. 2021.

[17] Q. Wang, J. Gao, W. Lin, and Y. Yuan, "Learning from synthetic data for crowd counting in the wild," in *Proc. IEEE Conf. Comput. Vis. Pattern Recognit.*, Jun. 2019, pp. 8198–8207.

[18] J.-Y. Zhu, T. Park, P. Isola, and A. A. Efros, "Unpaired image-to-image translation using cycle-consistent adversarial networks," in *Proc. IEEE Int. Conf. Comput. Vis.*, 2017, pp. 2223–2232.

[19] J. Hoffman *et al.*, "CyCADA: Cycle-consistent adversarial domain adaptation," 2017, *arXiv:1711.03213*.

[20] Y.-C. Chen, Y.-Y. Lin, M.-H. Yang, and J.-B. Huang, "CrDoCo: Pixel-level domain transfer with cross-domain consistency," in *Proc. IEEE Conf. Comput. Vis. Pattern Recognit.*, Jun. 2019, pp. 1791–1800.

[21] P. Viola and M. J. Jones, "Robust real-time face detection," *Int. J. Comput. Vis.*, vol. 57, no. 2, pp. 137–154, 2004.

[22] N. Dalal and B. Triggs, "Histograms of oriented gradients for human detection," in *Proc. IEEE Comput. Soc. Conf. Comput. Vis. Pattern Recognit. (CVPR)*, Jun. 2005, pp. 886–893.

[23] G. J. Brostow and R. Cipolla, "Unsupervised Bayesian detection of independent motion in crowds," in *Proc. IEEE CVPR*, vol. 1, Jun. 2006, pp. 594–601.

[24] D. Ryan, S. Denman, C. Fookes, and S. Sridharan, "Crowd counting using multiple local features," in *Digital Image Computing: Techniques and Applications*. Melbourne, VIC, Australia: IEEE, 2009, pp. 81–88.

[25] V. Lempitsky and A. Zisserman, "Learning to count objects in images," in *Proc. Adv. Neural Inf. Process. Syst.*, 2010, pp. 1324–1332.

[26] H. Idrees, I. Saleemi, C. Seibert, and M. Shah, "Multi-source multi-scale counting in extremely dense crowd images," in *Proc. IEEE Conf. Comput. Vis. Pattern Recognit.*, Jun. 2013, pp. 2547–2554.

[27] Y. Zhang, D. Zhou, S. Chen, S. Gao, and Y. Ma, "Single-image crowd counting via multi-column convolutional neural network," in *Proc. IEEE Conf. Comput. Vis. Pattern Recognit. (CVPR)*, Jun. 2016, pp. 589–597.

[28] D. Onoro-Rubio and R. J. López-Sastre, "Towards perspective-free object counting with deep learning," in *Proc. Eur. Conf. Comput. Vis.* Amsterdam, The Netherlands: Springer, 2016, pp. 615–629.

[29] V. A. Sindagi and V. M. Patel, "Generating high-quality crowd density maps using contextual pyramid CNNs," in *Proc. IEEE Int. Conf. Comput. Vis. (ICCV)*, Oct. 2017, pp. 1861–1870.

[30] W. Liu, M. Salzmann, and P. Fua, "Context-aware crowd counting," in *Proc. IEEE/CVF Conf. Comput. Vis. Pattern Recognit. (CVPR)*, Jun. 2019, pp. 5099–5108.

[31] J. Gao, Q. Wang, and Y. Yuan, "SCAR: Spatial-/channel-wise attention regression networks for crowd counting," *Neurocomputing*, vol. 363, pp. 1–8, Oct. 2019.

[32] J. Gao, Q. Wang, and X. Li, "PCC Net: Perspective crowd counting via spatial convolutional network," *IEEE Trans. Circuits Syst. Video Technol.*, vol. 30, no. 10, pp. 3486–3498, Oct. 2020.

[33] H. Idrees *et al.*, "Composition loss for counting, density map estimation and localization in dense crowds," 2018, *arXiv:1808.01050*.

[34] X. Jiang *et al.*, "Crowd counting and density estimation by trellis encoder-decoder networks," in *Proc. IEEE/CVF Conf. Comput. Vis. Pattern Recognit. (CVPR)*, Jun. 2019, pp. 6133–6142.

[35] L. Liu, Z. Qiu, G. Li, S. Liu, W. Ouyang, and L. Lin, "Crowd counting with deep structured scale integration network," 2019, *arXiv:1908.08692*.

[36] V. A. Sindagi, R. Yasarla, and V. M. Patel, "Pushing the frontiers of unconstrained crowd counting: New dataset and benchmark method," 2019, *arXiv:1910.12384*.

[37] Z. Yan *et al.*, "Perspective-guided convolution networks for crowd counting," in *Proc. IEEE/CVF Int. Conf. Comput. Vis. (ICCV)*, Oct. 2019, pp. 952–961.

[38] X. Liu, J. van de Weijer, and A. D. Bagdanov, "Leveraging unlabeled data for crowd counting by learning to rank," in *Proc. IEEE Conf. Comput. Vis. Pattern Recognit.*, Jun. 2018, pp. 7661–7669.

[39] D. B. Sam, N. N. Sajjan, H. Maurya, and R. V. Babu, "Almost unsupervised learning for dense crowd counting," in *Proc. 33rd AAAI Conf. Artif. Intell.*, vol. 27, 2019, pp. 8868–8875.

[40] G. Olmschenk, Z. Zhu, and H. Tang, "Generalizing semi-supervised generative adversarial networks to regression using feature contrasting," *Comput. Vis. Image Understand.*, vol. 186, pp. 1–12, Sep. 2019.

[41] M. Long, Y. Cao, J. Wang, and M. Jordan, "Learning transferable features with deep adaptation networks," in *Proc. Int. Conf. Mach. Learn.*, 2015, pp. 97–105.

[42] K. Bousmalis, G. Trigeorgis, N. Silberman, D. Krishnan, and D. Erhan, "Domain separation networks," in *Proc. Adv. Neural Inf. Process. Syst.*, 2016, pp. 343–351.

[43] M. Long, H. Zhu, J. Wang, and M. I. Jordan, "Deep transfer learning with joint adaptation networks," in *Proc. 34th Int. Conf. Mach. Learn.*, 2017, pp. 2208–2217.

[44] A. Gretton, K. M. Borgwardt, M. J. Rasch, B. Schölkopf, and A. Smola, "A kernel two-sample test," *J. Mach. Learn. Res.*, vol. 13, pp. 723–773, Mar. 2012.

[45] S. R. Richter, V. Vineet, S. Roth, and V. Koltun, "Playing for data: Ground truth from computer games," in *Proc. Eur. Conf. Comput. Vis.*, 2016, pp. 102–118.

[46] G. Ros, L. Sellart, J. Materzynska, D. Vázquez, and A. M. López, "The SYNTHIA dataset: A large collection of synthetic images for semantic segmentation of urban scenes," in *Proc. IEEE Conf. Comput. Vis. Pattern Recognit.*, Jun. 2016, pp. 3234–3243.

[47] J. Hoffman, D. Wang, F. Yu, and T. Darrell, "FCNs in the wild: Pixel-level adversarial and constraint-based adaptation," 2016, *arXiv:1612.02649*.

[48] S. Sankaranarayanan, Y. Balaji, A. Jain, S. N. Lim, and R. Chellappa, "Learning from synthetic data: Addressing domain shift for semantic segmentation," in *Proc. IEEE/CVF Conf. Comput. Vis. Pattern Recognit.*, Jun. 2018, pp. 3752–3761.

[49] T. Han, J. Gao, Y. Yuan, and Q. Wang, "Focus on semantic consistency for cross-domain crowd understanding," in *Proc. IEEE Int. Conf. Acoust., Speech Signal Process.*, May 2020, pp. 1848–1852.

[50] J. Gao, Y. Yuan, and W. Qi, "Feature-aware adaptation and density alignment for crowd counting in video surveillance," *IEEE Trans. Cybern.*, vol. 51, no. 10, pp. 1–12, Oct. 2020.

[51] A. Gonzalez-Garcia, J. van de Weijer, and Y. Bengio, "Image-to-image translation for cross-domain disentanglement," in *Proc. Adv. Neural Inf. Process. Syst.*, 2018, pp. 1287–1298.

[52] W.-L. Chang, H.-P. Wang, W.-H. Peng, and W.-C. Chiu, "All about structure: Adapting structural information across domains for boosting semantic segmentation," in *Proc. IEEE/CVF Conf. Comput. Vis. Pattern Recognit. (CVPR)*, Jun. 2019, pp. 1900–1909.

[53] B. Lu, J.-C. Chen, and R. Chellappa, "Unsupervised domain-specific deblurring via disentangled representations," in *Proc. IEEE Conf. Comput. Vis. Pattern Recognit.*, Jun. 2019, pp. 10225–10234.

[54] Y.-J. Li, C.-S. Lin, Y.-B. Lin, and Y.-C. F. Wang, "Cross-dataset person re-identification via unsupervised pose disentanglement and adaptation," 2019, *arXiv:1909.09675*.

[55] L. Hu, M. Kan, S. Shan, and X. Chen, "Duplex generative adversarial network for unsupervised domain adaptation," in *Proc. IEEE/CVF Conf. Comput. Vis. Pattern Recognit.*, Jun. 2018, pp. 1498–1507.

[56] Y. Cai, L. Chen, Z. Ma, C. Lu, C. Wang, and G. He, "Leveraging intra-domain knowledge to strengthen cross-domain crowd counting," in *Proc. IEEE Int. Conf. Multimedia Expo (ICME)*, Jul. 2021, pp. 1–6.

[57] X. Mao, Q. Li, H. Xie, R. Y. K. Lau, Z. Wang, and S. P. Smolley, "Least squares generative adversarial networks," in *Proc. IEEE Int. Conf. Comput. Vis. (ICCV)*, Oct. 2017, pp. 2794–2802.

[58] J. Johnson, A. Alahi, and L. Fei-Fei, "Perceptual losses for real-time style transfer and super-resolution," in *Proc. Eur. Conf. Comput. Vis.* Amsterdam, The Netherlands: Springer, 2016, pp. 694–711.

[59] K. Simonyan and A. Zisserman, "Very deep convolutional networks for large-scale image recognition," 2014, *arXiv:1409.1556*.

[60] D. P. Kingma and J. Ba, "Adam: A method for stochastic optimization," 2014, *arXiv:1412.6980*.

[61] J. Gao, W. Lin, B. Zhao, D. Wang, C. Gao, and J. Wen, "C^3 framework: An open-source pytorch code for crowd counting," 2019, *arXiv:1907.02724*.

[62] K. Chen, C. C. Loy, S. Gong, and T. Xiang, "Feature mining for localised crowd counting," in *Proc. Brit. Mach. Vis. Conf.*, 2012, p. 3.

[63] A. B. Chan, Z.-S. J. Liang, and N. Vasconcelos, "Privacy preserving crowd monitoring: Counting people without people models or tracking," in *Proc. IEEE Conf. Comput. Vis. Pattern Recognit. (CVPR)*, Jun. 2008, pp. 1–7.

[64] Z. Wang, A. C. Bovik, H. R. Sheikh, and E. P. Simoncelli, "Image quality assessment: From error visibility to structural similarity," *IEEE Trans. Image Process.*, vol. 13, no. 4, pp. 600–612, Apr. 2004.

[65] C. Zhang, K. Kang, H. Li, X. Wang, R. Xie, and X. Yang, "Data-driven crowd understanding: A baseline for a large-scale crowd dataset," *IEEE Trans. Multimedia*, vol. 18, no. 6, pp. 1048–1061, Jun. 2016.

[66] Q. Wang, J. Gao, W. Lin, and Y. Yuan, "Pixel-wise crowd understanding via synthetic data," *Int. J. Comput. Vis.*, vol. 129, pp. 1–21, Jan. 2020.

[67] H. Talebi and P. Milanfar, "NIMA: Neural image assessment," *IEEE Trans. Image Process.*, vol. 27, no. 8, pp. 3998–4011, Aug. 2018.

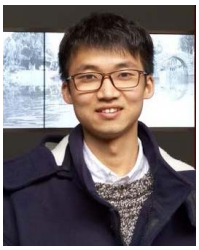

Junyu Gao (Member, IEEE) received the B.E. and Ph.D. degrees in computer science and technology from Northwestern Polytechnical University, Xi'an, China, in 2015 and 2021, respectively.

He is currently a Researcher with the School of Artificial Intelligence, Optics and Electronics (iOPEN), Northwestern Polytechnical University. His research interests include computer vision and pattern recognition.

Tao Han (Student Member, IEEE) received the B.E. degree in transportation equipment and control engineering from Northwestern Polytechnical University, Xi'an, China, in 2019, where he is currently pursuing the M.S. degree in computer science and technology with the School of Artificial Intelligence, Optics and Electronics (iOPEN).

His research interests include computer vision and pattern recognition.

Yuan Yuan (Senior Member, IEEE) is currently a Full Professor with the School of Artificial Intelligence, Optics and Electronics (iOPEN), Northwestern Polytechnical University, Xi'an, China. She has authored or coauthored over 150 papers, including about 100 in reputable journals, such as the IEEE TRANSACTIONS ON PATTERN ANALYSIS AND MACHINE INTELLIGENCE, as well as the conference papers in IEEE Conference on Computer Vision and Pattern Recognition (CVPR), British Machine Vision Conference (BMVC), International Conference on Image Processing (ICIP), and International Conference on Acoustics, Speech and Signal Processing (ICASSP). Her current research interests include visual information processing and image/video content analysis.

Qi Wang (Senior Member, IEEE) received the B.E. degree in automation and the Ph.D. degree in pattern recognition and intelligent systems from the University of Science and Technology of China, Hefei, China, in 2005 and 2010, respectively.

He is currently a Professor with the School of Artificial Intelligence, Optics and Electronics (iOPEN), Northwestern Polytechnical University, Xi'an, China. His research interests include computer vision and pattern recognition.